How do water and CO_2 impact the stability and emissions of the combustion in a micro Gas Turbine? — a Large Eddy Simulations comparison

Alessio Pappa[a,*], Marie Cordier[a], Pierre Bénard[b], Laurent Bricteux[a], Ward De Paepe[a]

[a] *University of Mons, Polytechnic Faculty, Mechanical Department, 7000 Mons, Belgium*
[b] *Normandie University, INSA Rouen, UNIROUEN, CNRS, CORIA, Rouen 76000, France*

Abstract

Micro Gas Turbines have to become more operational and fuel flexible, and carbon clean. Applying cycle humidification and Exhaust Gas Recirculation (EGR) in combination with Carbon Capture offers a solution. However, current advanced mGT cycle development is limited by the combustor. To improve the cycle performance further, stable and complete combustion has to be achieved under unconventional diluted conditions. Accurate data predicting the stability and performance of specific mGT combustors under these diluted conditions are still missing. A comparison between classic natural gas combustion in an mGT and three diluted cases with water and/or CO_2 using Large Eddy Simulations (LES) is presented in this paper. Results show that complete and stable combustion was reached for all cases. Although the flow dynamics are identical, diluted operating conditions lead to a wider reaction zone. An outlet temperature reduction could be observed in the water diluted cases due to the higher specific heat of the humidified combustion

*Corresponding author. Email: alessio.pappa@umons.ac.be

air. Regarding CO emissions, the humidified case presents slightly lower concentrations (25ppm) compared to the reference case (32ppm), while the dry EGR case shows the highest values (50ppm). Based on high fidelity LES results, the feasibility of mGT combustor operating under diluted conditions has been proven.
Keywords:
Large Eddy Simulation (LES), Turbulent Combustion, micro Gas Turbine (mGT), Humidified combustion, Exhaust Gas Recirculation (EGR)

---

1. Introduction

The more and more visible impact of climate change on our daily life together with the increasing awareness of the negative impact of air pollution on human health made that environmental issues have become the biggest concern of this century. The management of our energy resources and air pollution are strongly related to the combustion processes involved in transport, industry, domestic heating applications, and power generation. This last sector is responsible of 33.1 Gt of CO_2 emitted in the atmosphere in 2018 [1]. Whereas our current power generation and supply system has to support the growing energy demand while reducing drastically its CO_2 emissions [2], it also faces another challenge linked to the increasing implementation of renewable energy production. The unpredictable fluctuations of renewable energy sources, like wind and solar, put some severe constraints on the reliability and stability of the grid. Next to the integration of energy storage, shifting from centralized to a more decentralized, small-scale production, possibly in combination with Combined Heat and Power (CHP) production, can offer the

necessary flexibility to the grid to ensure stable and reliable production [3].

Considering these statements, micro Gas Turbines (mGTs) seem promising to fulfil the requirements of the future power generation market where the trend is indeed moving towards decentralized power production [3, 4]. With a typical net electricity generation ranging from 1 kW_e up to few 100 kW_e, while having typical efficiencies ranging 15 to 35% respectively, mGTs have a large field of application, especially in small-scale CHP production for residential and public applications, showing high total (combined electrical and thermal) efficiency combined with low CO_2 and NO_x emissions [5]. Although having a lower electrical efficiency than their main competitor, the Reciprocating Internal Combustion Engine (RICE), the mGT still has some advantages over the RICE, being lower maintenance costs, lower vibration levels, and less emission [6]. Nevertheless, mGTs did not really penetrate the market so far [7].

The adaptability of the mGT systems allows to perform cycle humidification, which enables a separated heat and power production control, leading to increased operational flexibility [8]. Indeed, in most CHP units, thermal and electrical power production are coupled, and their ratio is thus fixed. At the same time, for a typical residential user, the demand for electricity and heat is usually not linked, and can differ quite significantly (e.g., during summertime, when there is no demand for heat in residential applications). A lack of demand for heat always leads to a shut-down of the unit, given the moderate electrical efficiency (e.g., around 30% for the Turbec T100 [9], a typical mGT). During these periods, performing cycle humidification, and by doing so, re-injecting part of the thermal power back into the cycle, offers

a solution. Indeed, humidifying the mGT enables to increase the electric efficiency of the cycle and thus the operational flexibility of the unit, avoiding unnecessary shut-down, increasing so the economic profitability of the mGT [10, 11].

Cycle humidification can be achieved in several ways, going from simple steam injection to more advanced cycles using saturation towers and additional heat exchangers. A complete overview of the existing research on the humidified mGT cycles, and different cycle layouts is presented in [12]. The micro Humid Air Turbine (mHAT) in particular, introducing water in the cycle using a saturation tower, was identified as the most promising technology and its potential efficiency improvement was confirmed experimentally [8, 13, 14].

Next to improving the electrical performance, the high cycle adaptability also offers a solution to make the mGT carbon clean. mGTs are appreciated for their low carbon exhaust. However, to limit the effects of climate change, CO_2 emissions are still too high and need to be reduced rapidly. Applying Carbon Capture Utilization and Storage (CCUS) offers a solution to make the mGT carbon clean. However this require a high CO_2 concentration in the flue gases to keep the capture penalty low. Hence, performing Exhaust Gas Recirculation (EGR) on the mGT allows to achieve a higher CO_2 concentration in the exhaust gases, reducing thus the energy penalty linked with the carbon capture [15, 16]. One of the major impacts of EGR on the cycle is the reduced oxygen level in the oxidizer leading to possible flames instabilities [17]. Moreover this CO_2 enhancement involves an increase of the CO emissions as well as unburnt CH_4. Indeed, due to the displacement of oxygen, as well

as the increased heat capacity of the oxidizer (resulting from the altered composition) lower temperatures, reaction rates, and flame speed are observed in the combustion chamber [18].

Although EGR on mGT cycles reduces the carbon capture penalty, it has a negative effect on the cycle efficiency itself. Using cycle humidification (e.g., converting the mGT into an mHAT) can compensate these efficiency losses (allowing thus to perform CCUS with a higher efficiency). This solution was investigated by our research group [19, 20, 21], showing the impact of EGR on a flexible humidified mGT. This study revealed that mGT humidification increases the total cycle efficiency, entirely compensating the EGR induced losses. Humidifying the mGT with EGR opens thus a path for further investigation.

Although the different advanced cycle concepts have been proven effective in terms of mGT cycle performance improvement, the impact on the individual component performance, especially the combustion chamber, still remains an attention point. So, despite the high adaptability and the recent development on advanced mGT cycle modifications, it is clear that the combustion chamber remains the limiting factor for the full employment of the mGT potential. The mGT operation under diluted conditions can lead to a non-stable, incomplete combustion with increased CO emissions, negatively affecting the global cycle efficiency. It is thus essential to have detailed information on the combustion stability limits. Several experimental and numerical works on the assessment of the impact of water injection [10, 12, 22, 23, 24, 25] and of CO_2 dilution [15, 16] on the combustion performance and stability in mGTs, are available in the literature. However, most of these works only consider and describe

general trends clearly highlighting that the impact of such diluted working conditions is still too qualitatively studied, while a strong requirement for a more accurate turbulence modelling, such as Large Eddy Simulation, is identified. A major advantage of using LES is the possibility to analyse the instabilities captured by the Root Mean Square (RMS) of the different physical quantities (in RANS they are only modelled). Besides, numerical or experimental research on combustion at combined diluted conditions: i.e. at elevated CO_2 and H_2O concentration, as it is the case when combining both EGR and mHAT, is still missing. This lack of knowledge on the combustion process under these particular diluted conditions limits the technology progress towards more flexible operation.

The work presented in this paper aims at providing an accurate comparison, based on Large Eddy Simulations (LES), of the natural gas combustion process under different diluted (water and/or CO_2) conditions in a typical mGT, the Turbec T100. This comparison will allow to assess the impact of water injection, EGR or the combination of both on the combustion stability, efficiency and emissions. In this article, the advanced cycle modifications, including introduction of water and/or CO_2 in a typical mGT, the Turbec T100, is first described. Then the combustion chamber geometry and configuration are presented followed by the numerical set-up of the LES. Finally, the results based on a comparison of the stability, flame topology, flow fields, global performances, and emissions of the combustor are presented and discussed.

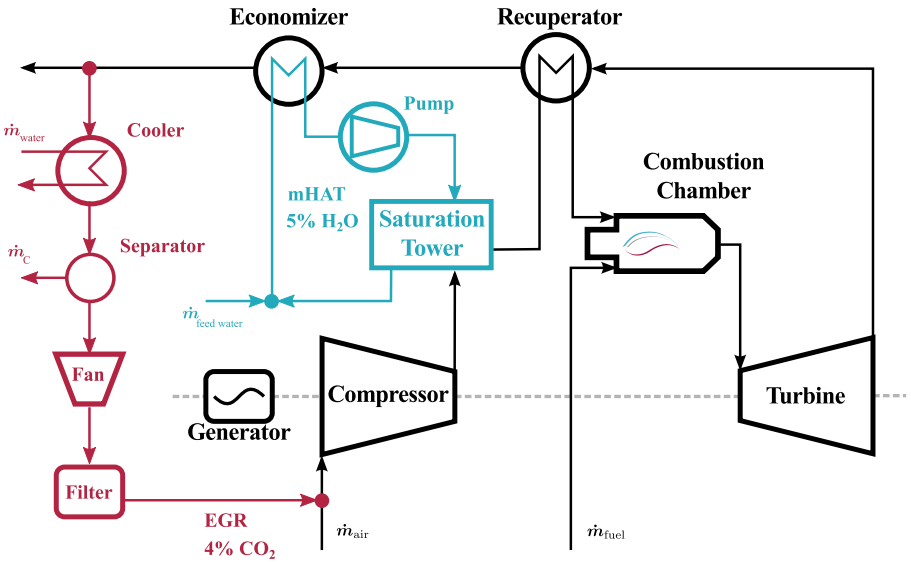

Figure 1: Typical recuperated mGT cycle (in black) with advanced modification for carbon capture penalty reduction and efficiency improvement such as humidification (mHAT, in blue) and EGR (in red).

2. Cycles description

Prior to the presentation of the LES set-up and results, it is essential to present the different considered mGT cycles. The cycles have been selected based on their major advantages and potential for carbon capture penalty reduction (EGR), cycle efficiency, and flexibility improvement (humidification), as demonstrated in recent works [12, 19, 20, 26]. The reference case as well as the advanced cycle modifications are based on the cycle of a commercial mGT, the Turbec T100 [9]. As shown in Fig. 1, the considered mGT cycles are: a typical recuperated mGT cycle (in black, reference case), a humidified cycle using a saturation tower (mHAT, in blue), a dry cycle with EGR (in red) and a humidified cycle with EGR (mHAT+EGR).

2.1. Typical recuperated mGT cycle layout

mGTs operate typically using the recuperated Brayton cycle. As shown by the black path in Fig. 1, the dry air is first compressed by the variable speed compressor. Then the compressed air is preheated by the recuperator using the heat from the exhaust gases before entering the combustion chamber to be heated further till 950 °C by burning fuel [8]. After combustion, the hot flue gases, at a pressure of approximately 4 bar, are expanded in the turbine to drive the compressor and to produce electrical power using the generator. Finally, the heat of the flue gases is first used to preheat the incoming air in the recuperator, and then the remaining heat is used for thermal power production by heating water in the economiser.

2.2. Humidified mGT cycle layout

The recuperated mGT can be converted into an mHAT by adding a saturation tower between the compressor outlet and the recuparator inlet. Considering the blue path in Fig. 1, the compressed air coming from the compressor is humidified in the saturation tower by injecting an excess of hot water in the saturation tower. Part of the water (approximatively 5 % in mass) is evaporated using the heat available from the excess water. After humidification, the saturated pressurised air is again preheated by the recuperator using the flue gases, and heated further in the combustion chamber. The main difference with the typical recuperated mGT cycle is that no thermal power remains available after preheating the water for humidification. Indeed, the remaining heat in the exhaust gases is used to heat the water that will be sprayed into the saturation tower to humidify the

incoming compressed air. Finally, the evaporated water is replaced with feed water.

2.3. Dry and wet mGT cycle with EGR

EGR is performed on the dry or humidified mGT cycle by spliting a part of the exhaust gases, and reinjecting it in the compressor inlet, as shown by the red path in Fig. 1. Part of the exhaust gases are recirculated to the compressor inlet: first the gases are cooled down, then condensed water is separated from the gases, and finally blowed by a fan through a filter up to the compressor inlet. Besides the altering composition of the inlet air, the main working fluid pathway of the mGT or mHAT remains unaffected and similar to the reference case.

3. Combustion chamber configuration

The considered mGT combustor has been inspired on the combustion chamber of the Turbec T100 mGT [9] which features a can swirl burner layout (Fig. 2). The particularly challenging mesh generation for industrial gas turbine combustors, due to the geometrical complexity, requires simplification with respect to the actual geometry. Therefore, the complex geometry of the original burner (Fig. 2) has been adapted to a simplified cylindrical layout, as presented in Fig. 3, for the LES. Despite the simplification, this generic geometry offers flexibility, and still allows to assess the general trends, required by the main goal of this paper. Moreover, this geometry allowed to determine successfully the impact of H_2O addition on H_2 combustion stabilization [27].

In this layout, the typical characteristics of the real combustor geometry, such as the length of three times the chamber diameter D, as well as the two

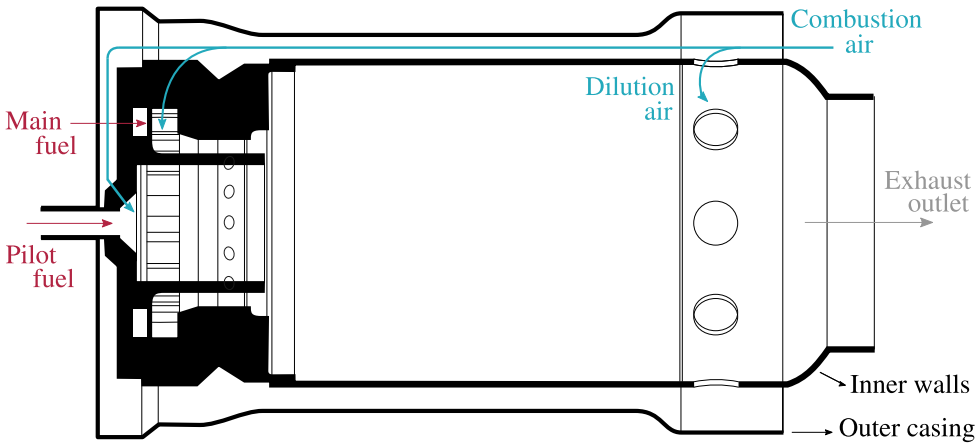

Figure 2: The Turbec T100 combustion chamber is a reverse (or counter-current) flow can burner where the combustion air is entering between the outer casing and the inner walls of the combustor. The air reaches then the dilution holes, the pilot, and main injectors by passing on the external surface of the inner walls.

flames, pilot and main, have been conserved. As in the Turbec T100 mGT, the pilot flame is a diffusion flame, fed by 12 air injectors ($d_{inj,air}/D = 0.033$, with $d_{inj,air}$ the diameter of the pilot injectors for air and D the diameter of the combustor) and 6 fuel injectors ($d_{inj,fuel}/D = 0.004$, with $d_{inj,fuel}$ the diameter of the pilot injectors for fuel). For the main flame, which is a premixed flame, the original T100 geometry has two swirlers. The first one is located upstream to premix fuel and air through 15 guide vanes. The second one, located downstream and closer to the combustion chamber, offers a swirled dynamic to the flow, and is adding more air to the mix just before entering the combustion chamber through 30 guide vanes. To reduce the computational cost, the designed layout for the simulations presented in this paper has been adapted to use only the downstream 30 injectors with $d_{inj,main}/D = 0.05$ (with $d_{inj,main}$ the diameter of the main injectors, Fig. 3).

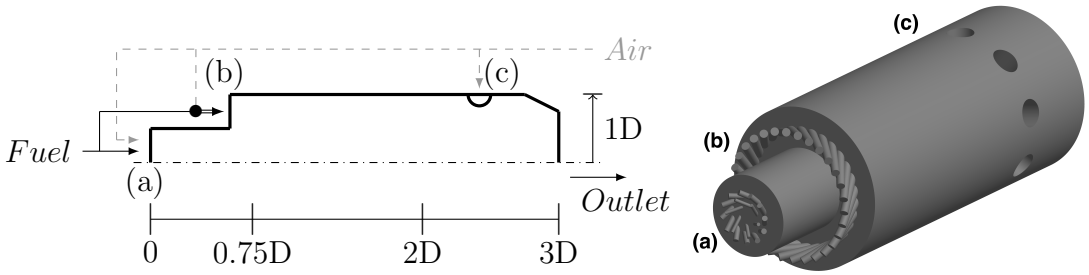

Figure 3: The simulation domain is defined by the inner walls of the combustion chamber where the total combustion air flow rate is distributed as follows: 5 % in the 12 pilot injectors (6 for fuel and 6 for air) for the diffusion flame (a), 30 % in the 30 main premixed injectors (b) and 65 % through the 9 dilution holes (c).

As previously shown by the authors of this paper using LES simulations [28], this change has no impact on the velocity field. In order to limit the temperature of the flue gases entering the turbine (to 950 °C), the hot gas is diluted using 9 dilution holes (DH) (Fig. 2), which have also been adopted in the geometry used for simulations (Fig. 3). In the original geometry (Fig. 2), the fresh combustion air, passing on the outside of the burner, is preheated by the convective heat transfer with the reaction zone. In the LES simulations, the outer casing walls of the can are not modelled (to reduce the mesh size and the computational cost), but the convective heat flux through the inner walls is simulated using a wall cooling model, and the combustor inlet air temperature was thus changed accordingly.

Since the geometry is based on the Turbec T100 combustion chamber, we opted to use operating conditions as close as possible as those found in the T100 for the dry reference mGT case [29]. The working conditions are chosen such that the air-to-fuel equivalence ratio of the reference case corresponds to the actual ratio of the T100, while the thermal power, injected in the chamber

Table 1: Operating conditions of the generic combustion chamber for mGT applications.

Total oxidizer mass flow rate [g/s]	400
Pilot fuel injector mass flow rate [g/s]	0.7
Main fuel injector mass flow rate [g/s]	4.2
Pressure [bar]	4
Fuel inlet temperature [K]	288
Air inlet temperature [K]	865
Thermal power [kW]	242

by the fuel, is kept constant for all the four cases. Although, according to the technical datasheet of the T100 provided by the manufacturer [9], the mGT has an air mass flow rate of 0.8 kg/s when operating at nominal power output of 100 kW, we opted to use a reduced combustion air mass flow rate of 400 g/s entering the chamber at 590 °C and 4 bar. Although the T100 is able to operate with an air flow rate in a range from 600 g/s and 800 g/s (depending on the operating point) by varying the rotational speed of the compressor, as shown in [10, 29], the geometry used in this paper requires a lower air flow rate to ensure that the velocities and the equivalence ratio in the chamber are similar to those of the reference chamber (typically 120 m/s in the main injectors [15]). So rather than injecting 600 g/s, a reduced total air mass flow rate of 400 g/s is injected in the combustion chamber, distributed over the different injectors and dilution holes as follows (see Fig. 3): 65 % of the mass flow rate enters the chamber through the dilution holes, 30 % with the main premixed injectors, and 5 % in the pilot injectors [15, 30, 31].

Table 2: Mass fraction Y_k [·] of the fuel and combustion air composition at the inlet for each case: typical mGT cycle, humidified cycle, dry cycle with EGR, and humidified cycle with EGR. The compositions are based on ASPEN simulations from the different cases [19].

		CH_4	C_2H_6	CO_2	N_2	O_2	H_2O
Fuel	All cases	0.914	0.05	0.014	0.022	-	-
Air	Reference	-	-	-	0.7679	0.2321	-
	mHAT	-	-	-	0.755	0.195	0.05
	Dry EGR	-	-	0.04	0.76	0.2	-
	Humid EGR	-	-	0.04	0.74	0.17	0.05

Given this lower combustion air flow rate, the considered geometry requires also a reduced fuel consumption of 240 kW with respect to the 330 kW for the original T100 chamber.

Since the aim of this paper is to assess the impact of H_2O and CO_2 dilution of the combustion air, as a result of advanced cycle modifications, on the combustion performance, simulations are performed using altered combustion air compositions. As mentioned before, the considered mGT cycles are (Fig. 1): a classical typical recuperated cycle (reference case in black), a humidified cycle using a saturation tower (mHAT, in blue), a dry cycle with EGR (in red) and a humidified cycle with EGR (mHAT+EGR). For the diluted cases, the cycle modifications lead thus to an additional mass fraction of 5 % of H_2O for the humid cases [32] and 4 % of CO_2 for the cases with EGR [15]. For each case, the simulations were performed with a constant fuel flow rate, meaning operation at constant thermal power injection was assumed, which is slightly

different than the actual mGT, that operates at constant TOT. All operating conditions for the studied cases are summarized in Table 1 and Table 2. From these tables, it is clear that the different cycle modifications stand out by a modification of the combustion air. Indeed, water and/or CO_2 are added to the cycle upstream of the CC, involving thus a shift from 0.232 to 0.292 for the fuel-air equivalence ratio (Table 3). The different combustion air inlet compositions are based on ASPEN Plus® simulations for the different cases [19].

4. Numerical set-up

Since the swirled injection leads to a flow with strong shear regions and high turbulence level, performing scale-resolved simulations provides a better understanding of the flow behaviour compared to a classical RANS approach. In this framework, the LES, presented in this paper, are performed using the massively parallel flow solver YALES2 [33]. This finite-volume code solves the low-Mach number Navier-Stokes equations using a projection method for variable density flows. Equations are solved using a $4^{\,\text{th}}$ order centred scheme in space and a $4^{\,\text{th}}$ order Runge-Kutta-like scheme in time [34]. The numerical code has been validated several times for different configurations [35, 36]. Especially, the validated LES of the lean-premixed Preccinsta burner with wall heat loss is comparable to our case [37].

The mesh of the complex geometry of the mGT combustor includes 33.125 million tetrahedral cells where the cells size in the main injectors is $\Delta = 250\,\mu\text{m}$ ($\Delta/d_{inj} = 0.042$). The turbulent sub-grid scale stresses are modelled with the local dynamic Smagorinsky model [38]. The stability of

the time integration is ensured with an adaptive time step that keeps the CFL number under 0.4. Moreover, the selected operating conditions involve a Reynolds Number Re = 20000 and a dimensionless wall distance $y^+ = 45$ in the main injectors. If the wall grid resolution is such that $y^+ > 30$, a wall model is required. In our simulations, we use a classical log-law profile as wall model [39]. For all cases, the simulation ran over 12 convective times ($T_{cv} = 3\mathrm{D}/\langle U_{CC}\rangle$ with $\langle U_{CC}\rangle$ the mean velocity of the flow in the combustion chamber) to ensure that the flow is well established. An additional 4 T_{cv} were used to obtain the statistics presented in this paper. The total of 16 T_{cv} required 215 000 CPUh.

As shown in Fig. 3 and discussed in previous section, the simulation domain is limited to the inner flow section of the combustion chamber. The reverse flow in the outer casing (see Fig. 2) is not simulated, however non-adiabatic conditions are considered for the walls. The wall cooling effect of the external reverse flow is simulated using a Neumann condition. An exchanged heat flux of 6 kW is imposed on the walls of the combustion chamber. This convective heat transfer was obtained out of energy balance calculations with experimental temperature measurements [8, 31].

The LES of the combustion were performed coupling finite-rate chemistry to a detailed chemical mechanism. The conservation equations for reacting flows (mass, species, momentum and energy) are solved by transporting all species of the chemical mechanism and evaluating the source terms from the kinetic mechanism. The kinetic scheme DRM19 (21 species and 84 reactions) is used [40]. A comparison between the DRM19 and the detailed kinetic mechanism GRI-3.0 (53 species and 325 reactions [41]) has been established for

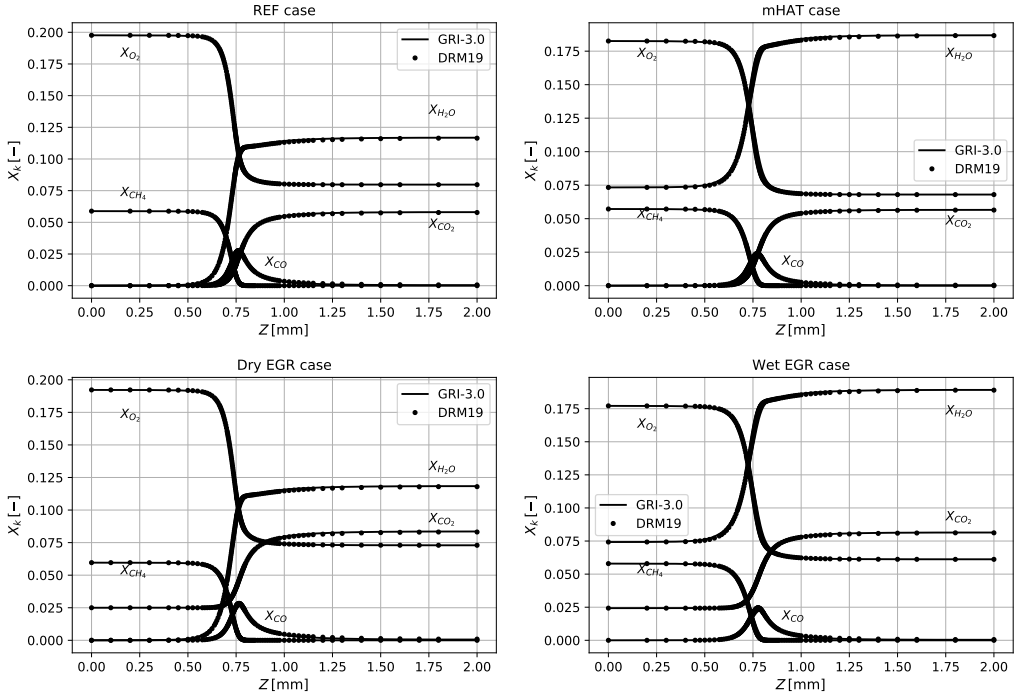

Figure 4: 1D laminar flame simulations with both kinetic scheme, DRM19 and GRI3, showing identical results for the species evolutions for all considered cases.

each case. This comparison is performed using a 1D laminar flame calculation where the results of the evolution of the different species are consistent and identical for both kinetic schemes and all operating conditions defined by the different cases. Fig. 4 shows that the DRM19 provides similar results compared to the GRI-3.0 for every case, but at a reduced cost.

To ensure that the mesh is fine enough to correctly capture the flame front, the thermal thickness of the laminar flame is compared with the mesh size in the reaction area. By simulating the theoretical unstrained 1D flame for all different cases using the same operating conditions, the thermal flame thickness could be calculated. Table 3 shows that the flame thickness (δ_L^0)

Table 3: Equivalence ratio, laminar flame velocity and flame thickness comparison between the different cases show that combustion air dilution has only a minor effect.

	ϕ [-]	S_L^0 [m/s]	δ_L^0 [µm]
Reference	0.232	1.387	350
mHAT	0.2644	1.191	400
Dry EGR	0.2596	1.228	380
Wet EGR	0.292	1.003	458

is ranging from 350 µm to 458 µm, while the cell size in the region of the injectors near the flame front ranges from 250 µm up to 1000 µm, which will lead to under-resolved source terms of the species. The cells size of the mesh is thus not refined enough to ensure the direct resolution of the combustion in the flame front. In this framework, a combustion model of artificially thickened flames is used to predict correctly the combustion and to model the sub-grid scale turbulence/chemistry interaction on the LES grid. In our LES, the Dynamic Thickened Flames model (DTFLES) [42] is implemented by modifying the conservation equations with a thickening factor F and the efficiency function E of Charlette et al. [43] (considering a static formulation with $\beta = 0.5$), to have the thermal flame thickness $\delta_T = F \cdot \delta_L^0$ and flame speed $S_T^0 = E \cdot S_L^0$ where S_T^0 is the sub-grid scale turbulent flame speed [44]. This model is suitable for premixed flame as well as for non-premixed flame since the dynamic formulation of the TFLES model is implemented in YALES2. In this dynamic formulation of the TFLES model, the thickening factor is not constant in the domain as proposed and showed by Légier et al. [45] and

Schmitt et al. [46] in their extended model to non-premixed flames. Therefore, the combination of the flame sensor, to track the region where the combustion takes place, with a non-constant thickening factor, makes the model suitable for both premixed and non-premixed flames. Finally, the authors of this work would like to stress that the TFLES model is now a well-know and several times validated model in the literature, for a various range of application [37, 43, 44, 45, 46, 47]. However, Bénard et al. [37] showed that the CO prediction remains difficult in LES (combustion model considered or not). Indeed, the accuracy of the prediction is related to a fine mesh resolution in addition with the model of wall heat transfer. Hence, the CO overestimation is a well-know problem when using the TFLES model. Therefore, the main trend of the CO evolution between the different cases is mainly analysed.

5. Results

In this section, the results obtained for the LES of the swirled flow in the mGT combustor, considering the 4 different cases including the reference case (typical recuperated mGT cycle), the humidified case, and the both dry and wet EGR cases, are analysed. The global performance of the burner in normal and diluted conditions is studied with a qualitative approach, using stability, flame topology and flow fields. Additionally, a quantitative analysis on the emissions is presented as well.

5.1. Stability and flame topology

Swirled burners are widely used in gas turbine, and mGT in particular, given their enhanced flame stability. Indeed, they promote recirculation inside the combustion chamber [44]. When the geometry of the injectors results in a

Swirl number S higher than 0.6, the flow shows an Inner Recirculation Zone (IRZ) and an Outer Recirculation Zone (ORZ) (Fig. 5) generated by the rapid expansion of the swirling flow in the combustion chamber. By reintroducing hot products in the reactive zone as a result of the high recirculation rate, flame stabilization is promoted, which leads to extended flammability limits [44]. Hence, the geometry is set up for a Swirl number [47, 48]:

$$S = \frac{G_\theta}{R \cdot G_z} = \frac{\int_0^R \rho\, u_z\, u_\theta\, r^2\, dr}{R \int_0^R \rho\, u_z^2\, r\, dr} = 0.707, \tag{1}$$

at the main injection considering an injection angle of $\theta = 45°$, where this definition compares the axial flux of tangential momentum G_θ to the axial momentum flux G_z with R the outer radius of the cylindrical injector. The streamlines from the time-averaged velocity $\langle \mathrm{U} \rangle$, shown in Fig. 5, allow to highlight the development of the ORZ and IRZ in the combustion chamber. A first ORZ and IRZ stand out in the pilot diffusion flame region where the main stream between these both recirculation zones joins downstream the centerline stream in the main part of the combustor. Additionally, the main premixed flame also develops a toroidal ORZ generated by the rapid expansion of the swirling flow and confined by the walls of the chamber. The IRZ of the main flow is stretched by the ORZ and is led by the centerline stream coming from the pilot flame. The centerline stream is accelerated by the swirling stretched IRZ due to the exchange of momentum.

A first indicator to analyse flame stability and topology in a qualitative way is using the 3D heat release visualisation. Indeed, as illustrated by Fig. 6, the iso-contour of the time-averaged heat release is compared for the reference case, mHAT case, and both dry and wet EGR cases at the same

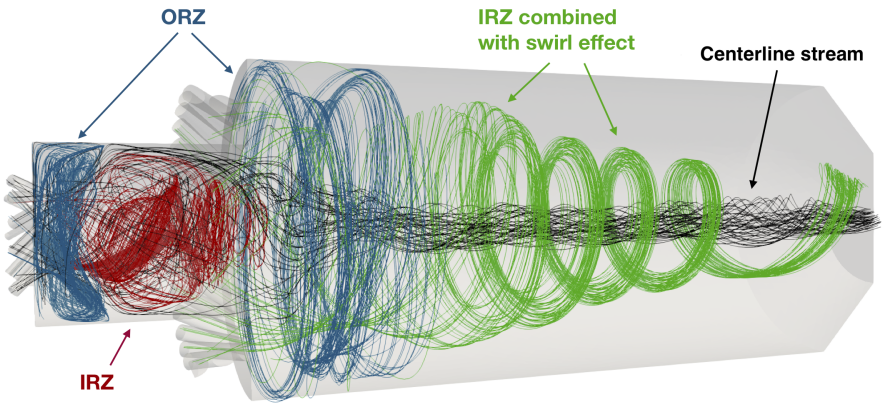

Figure 5: The streamlines from the time average velocity $\langle U \rangle$ allow to highlight the development of the Outer Recirculation Zone (ORZ) and Inner Recirculation Zone (IRZ).

value ($5 \times 10^8\,\mathrm{W/m^3}$). For this level of heat release, the 3D visualisation of the flame front appears more stable and better attached for the reference case whereas the dry EGR case shows a lower and smaller flame front. Furthermore a clearly less developed flame front for this level of heat release can be observed for the both humid cases (mHAT and mHAT+EGR). Although the analysis does not allow to discuss the full flame stability, we can conclude that the humid cases raise a flame with a lower heat release, but certainly a more spread reaction along the CC as will be shown in Fig. 11.

The temporal fluctuation of the thermal power released by the reaction in the combustor gives an additional clue for the stability assessment. Indeed, Fig. 7 allows to compare the time evolution over four convective times T_{cv} of the dimensionless ratio of the computed thermal power P_r released by the

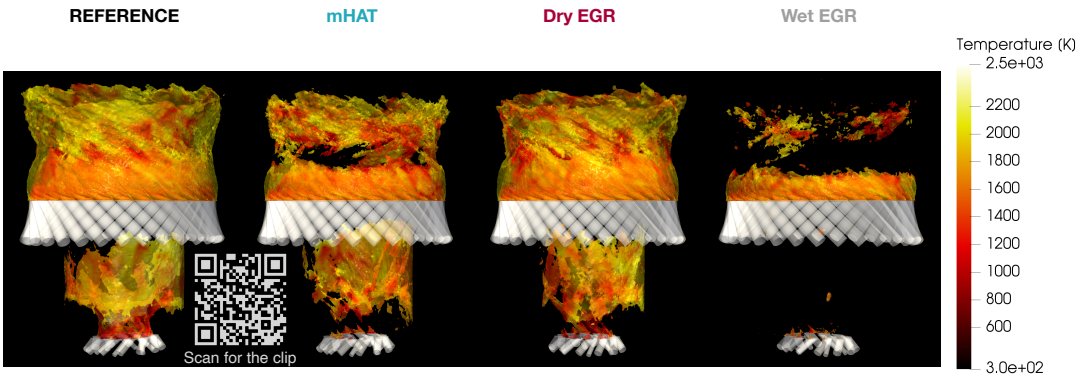

Figure 6: The iso-surfaces of the time-averaged heat release allow to compare the flame front of the reference, the mHAT, and both dry and wet EGR cases (from left to right).

reaction over the theoretical power of the combustor P_{in}:

$$P_{in} = \dot{m}_{fuel} \cdot \mathrm{LHV} \tag{2}$$

$$P_r = \int_V \dot{\omega}_T \, dV, \tag{3}$$

where LHV is the Lower Heating Value of the fuel, and $\dot{\omega}_T$ the reaction rate. We can observe in Fig. 7 that there are only limited fluctuations around the ratio $P_r/P_{in} = 1$, involving a stable and complete combustion for all cases. Indeed, when looking at the Table 4, we can conclude that the combustion is stable for all considered cases, since the average value of the ratio P_r/P_{in} is close to 100 % and shows a maximum standard deviation of the fluctuations of 2.9 %.

Flame stability and topology analysis showed that the diluted cases present the same flow dynamic as the reference case with the appearance of ORZ and IRZ in the same region, and similar velocity and TKE profiles. However, lower peaks of heat release and a more spread reaction are observed in the diluted cases compared to the reference case. Finally, the results showed that

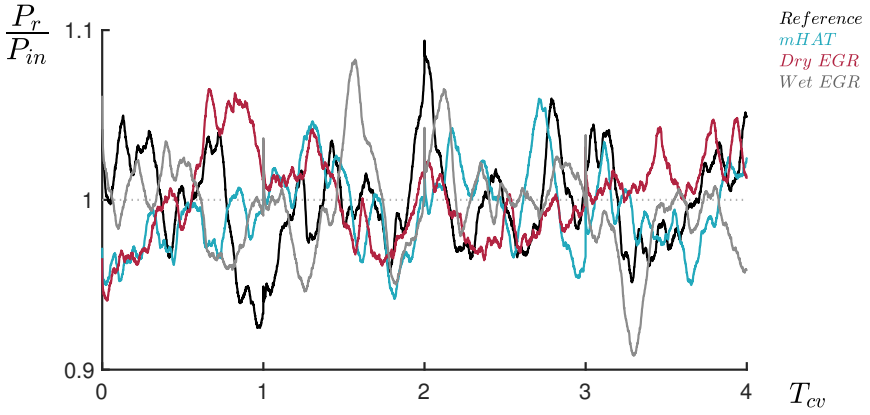

Figure 7: Time evolution of the dimensionless thermal power P_r over the power of the combustor P_{in} for stability comparison shows that the combustion is stable for all considered cases with a maximum deviation of the fluctuation of less than 10 %.

stable combustion is achieved for all considered cases with minor fluctuations of the thermal power produced by the combustor.

5.2. Flow fields comparison

In this section, the LES results of the different cases are analysed and compared in a qualitative approach using 2D cross-sectional color maps along the axial axis. These color maps only show the reaction area (region

Table 4: Comparison of the released thermal power and its fluctuation in the combustion chamber under diluted conditions shows only limited fluctuations around the ratio $P_r/P_{in} = 100\%$ with a maximum standard deviation of 2.9 %, indicating stable combustion is achieved for all cases.

	Reference	mHAT	Dry EGR	Wet EGR
Mean value P_r/P_{in} [%]	99.94	99.39	100.23	99.57
Standard deviation P_r/P_{in} [%]	2.89	2.41	2.57	2.84

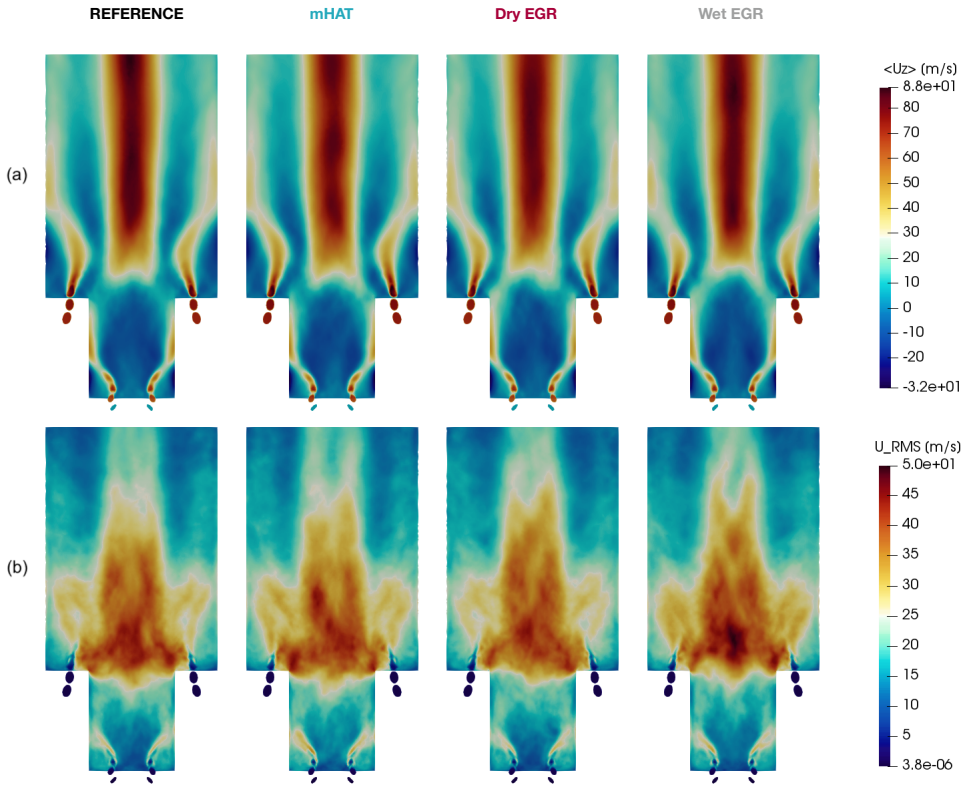

Figure 8: 2D cross-sectional color maps of the time-averaged axial velocity (a) and time-variation (b) show no significant differences between the cases, but allow to highlight the recirculation areas.

of interest), not showing the dilution holes (DH) and outlet regions (until $Z = 2D$ on Fig. 3).

As expected, the time-averaged (Fig. 8 (a)) and RMS velocity fields (Fig. 8 (b)) are very similar for the four cases. Indeed, we did not expect that the applied modifications of the air composition would have an impact on the flow dynamic given the relative small changes in the composition (5% H_2O and 4% CO_2 addition). The influence of different combustion air composition on

the flow structure remains minor given the high Reynolds number. These results show that the flow is well established in the combustion chamber (first clue for stable combustion for each case), and the symmetrical shape of the time-averaged and time-variation fields ensure that the simulations run over sufficient convective time. Furthermore, the recirculation area of the flow is clearly visible in Fig. 8 (a) (the blue to dark blue regions (0 to $-32\,\mathrm{m\,s^{-1}}$)) highlight the reverse flow with negative velocity values, affording then the conclusion exposed in the previous section. Given this choice of color scaling, the area of reverse flow are highlighted with the negative values of velocities (these results converge with the conclusions of the previous section).

The time-averaged distribution of the temperature (Fig. 9 (a)) shows that a global lower level of temperature is reached in both wet cases, especially in the region beneath the flame front in comparison with the reference case. For the dry CO_2 dilution, a temperature decrease is also observed, however, less pronounced. The temperature levels are the lowest for the wet EGR case, suggesting that combined EGR with H_2O addition would generally reduce the NO_x emissions compared to the dry ref case and even below the level of the mHAT and dry EGR cases. Regarding the RMS variation (Fig. 10 (a)), water and CO_2 addition show to have no significant impact on the temperature variation for the main flame, involving thus no additional perturbation on the temperature field and on the combustion stability. Nevertheless, the variations are slightly less intense in the region of the pilot flame for the wet EGR case in comparison to the reference case case, and to a lesser extend for the mHAT and dry EGR cases, leading thus to more stability.

When looking at both the time-averaged (Fig. 9 (b)) and RMS heat release

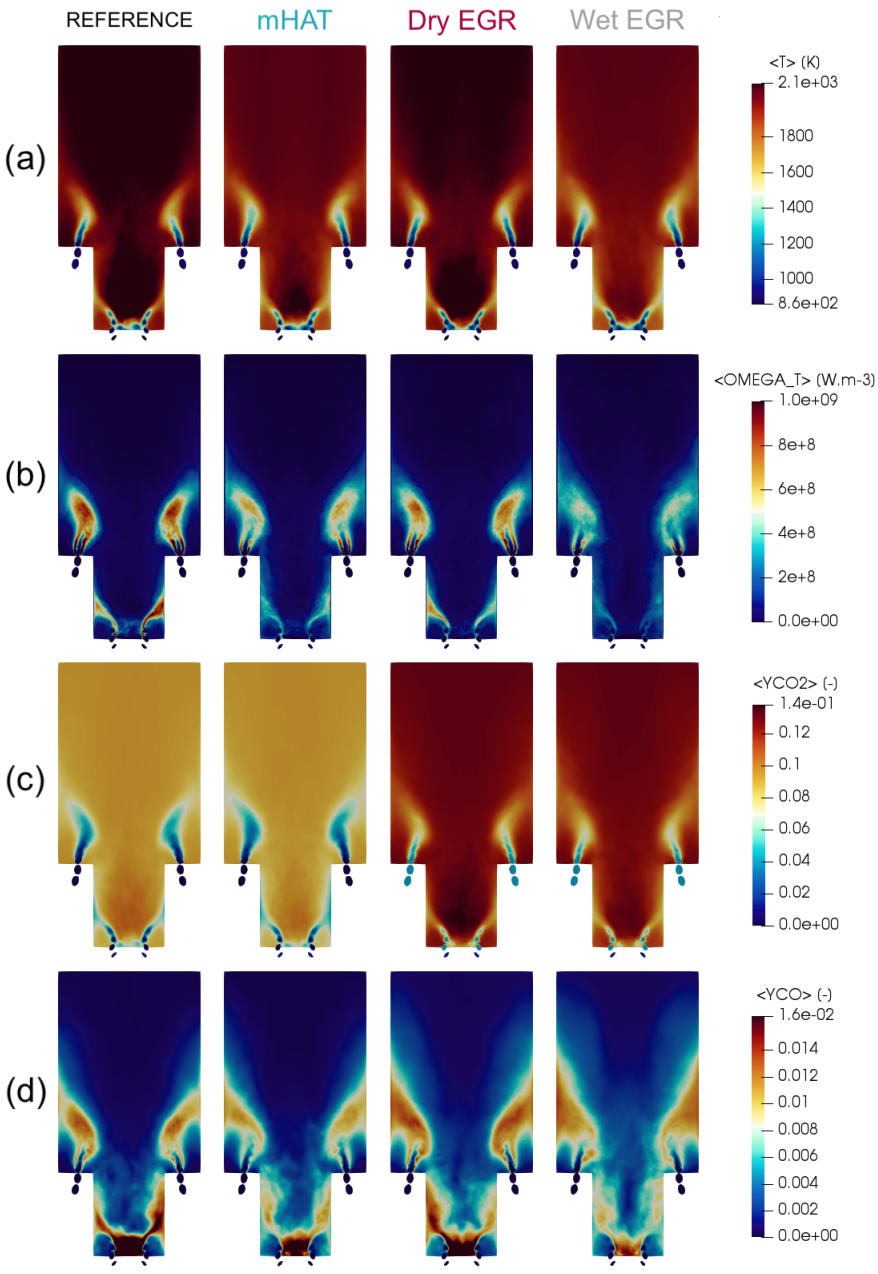

Figure 9: The effect of water and/or CO_2 addition on the combustion can be observed on the time-averaged 2D cross-section color maps of the temperature (a), reaction rate (b), CO_2 (c) and CO (d) concentration taken along the axial axis for the reference, mHAT and both dry and wet EGR cases.

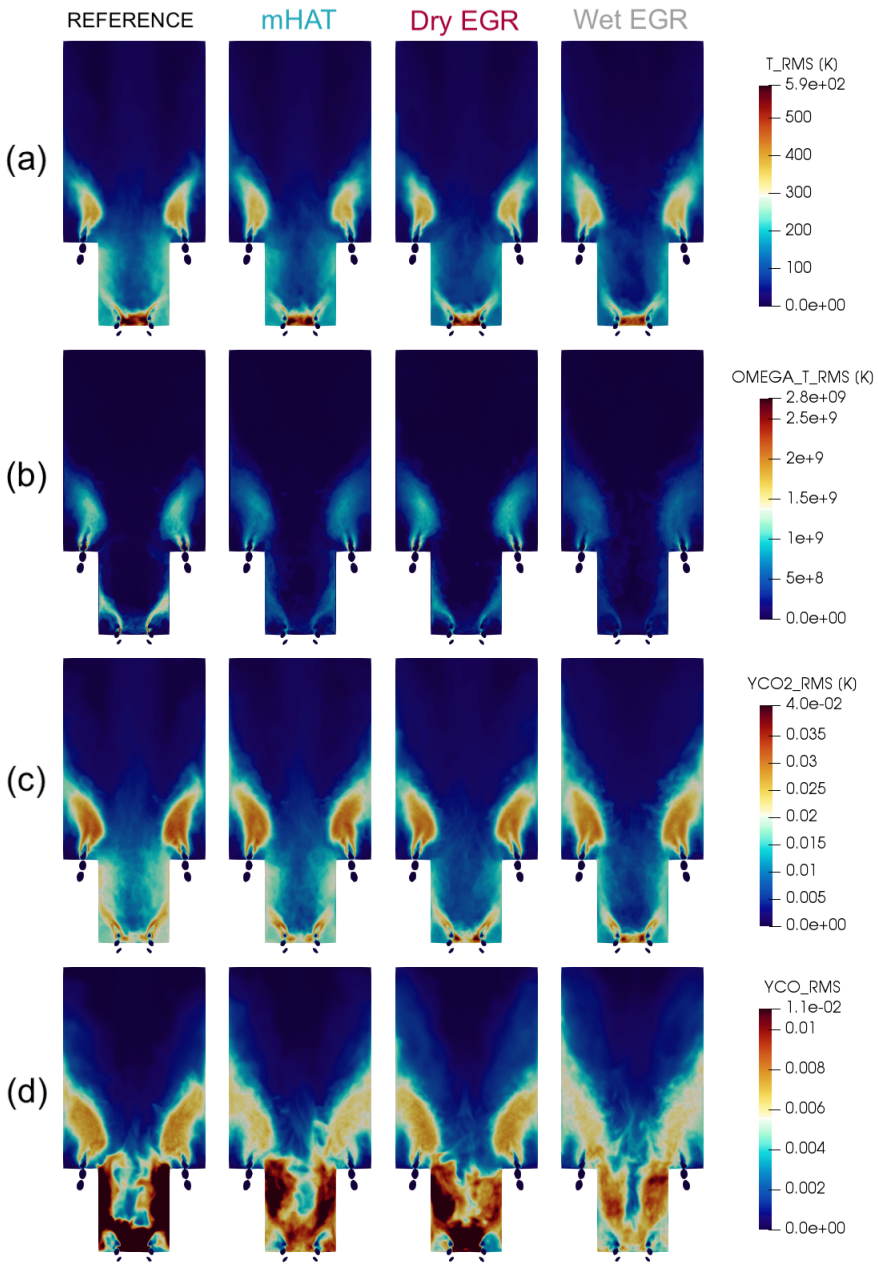

Figure 10: The effect of water and/or CO_2 addition on the combustion stability can be observed on the time-variation (RMS) 2D cross-section color maps of the temperature (a), reaction rate (b), CO_2 (c) and CO (d) concentration taken along the axial axis for the reference, mHAT and both dry and wet EGR cases.

(Fig. 10 (b)), we can clearly observe that the mHAT and both dry and wet EGR cases show a slight wider reaction zone with lower maximal values, compared to the more intense reaction in the reference case. The reaction rate for both humidified cases is clearly lower than the heat release of the reference case, and to a lower extend the dry EGR case, with a time-averaged value around $6 \times 10^8\,\mathrm{W\,m^{-3}}$ against $9 \times 10^8\,\mathrm{W\,m^{-3}}$ in the flame region. Moreover, the color map of the reaction rate of the reference case shows also a smaller fresh gases zone in the flame front, while diluted cases result in a wider reaction area. In addition, humidification does not only prevent peaks of reaction, it also reduces the heat release variations (Fig. 10 (b)), resulting in similar levels for both humid cases, leading therefore to a more stable combustion. In these simulations, we worked with low H_2O content in the combustion air while more variations are expected when going to higher levels of H_2O dilution.

Regarding the CO_2 mass fractions, we can observe that the results show similar trends along the radial axis of the combustion chamber (Fig. 9 (c)). On the one hand, the reference dry mGT and mHAT cases, having no CO_2 in the combustion air, produce same order of magnitude of CO_2 emissions. On the other hand, both dry and humid EGR cases result in higher CO_2 levels in the exhaust gases. Since these cases operate with a higher CO_2 content of the combustion air entering the chamber, outgoing levels must be higher. Correcting for the initial $4\,\%$ CO_2 in the combustion air as a result of the flue gases recirculation in the EGR cases, the same range of CO_2 emissions are reached for all cases. Regarding the distribution of the RMS CO_2 levels, similar results are observed for all cases. Hence, we can conclude that water addition,

considering a limited fraction, does not have any effect on CO_2 emissions, and the EGR with CO_2 dilution neither, since in both cases, complete combustion was still achieved. This trend was also found by De Santis et al. [15].

For the time-averaged distribution of the CO concentration (in mass fraction) in the chamber (Fig. 9 (d)), the same conclusion made for the heat release analysis can be drawn for the CO: in general, the CO levels are relatively low in the chamber, and the highest levels are mainly located near the flame front with a slightly wider distribution for the diluted cases. Whereas an increase in CO levels might be expected for both humidified cases due to lower temperature levels, on the contrary a slight decrease is observed for the mHAT case. An explanation can be found in the relative low H_2O addition, limiting this effect. When going to higher H_2O fractions, a more profound impact is expected. Additionally, as expected, in regard to the higher initial CO_2 content, a slight increase of CO concentration is observed for the dry EGR with higher peak levels. The most pronounced CO increase is however linked to the wet EGR. Although the wet EGR case shows only the same levels of CO peak emissions as the reference case in the flue gases. However the distribution is far more spread, increasing the total quantity compared to the reference case. This conclusion is confirmed using a volume integral on the domain to obtain qualitative values, as presented in more details in the next section on the prediction of the flue gases emissions. Finally, the time-variation comparison (Fig. 10 (d)) shows that both conjugated effects of water and CO_2 dilution have a significative impact of the CO time-variation where the distribution is less concentrated and more spread in the combustion chamber with lower peaks of production for the wet EGR case. This trend is,

to a lower extend, also observed with the mHAT case, while the dry EGR shows a similar profile as the reference case.

5.3. Prediction of the flue gas emissions

The comparison of the performances and the emissions of the combustor are characterized using the azimuthal average profiles of temperature, reaction rate, and mass fractions of CO_2 and CO at 3 axial positions along the chamber: in the region of the flame front at $Z = 0.75D$, before the DH at $Z = 2D$, and at the outlet $Z = 3D$ (see Fig. 3). The time-averaged and the RMS quantities are studied for the reference case (in black), the humidified cycle (in blue), and both dry (in red) and wet (in grey) EGR cycle. Fig. 11 represents the temperature and the dimensionless heat release profiles, while the profiles of the mass fraction of the CO_2 and CO profiles are presented in Fig. 12. Finally, we wanted to stress that the x-axis is not kept constant for each plane to better highlight the shape of the different profiles.

When looking at the evolution of the temperature along the radial axis (y-axis) for the different positions in the combustion chamber (Fig. 11 (a)), a constant shift from 50 K up to 80 K along the chamber from the flame front ($Z = 0.75D$) to the DH ($Z = 2D$) can be observed between the dry and humid cases. This shift is a result of the higher specific heat of the combustion air due to the water addition. This discrepancy slightly decreases to maximum 30 K after the DH. At plane $Z = 3D$ of each profile, as mentioned before, combustion air is injected in the combustion chamber to lower the turbine inlet temperature to lower the thermal fatigue and to avoid mechanical failure. This dilution is responsible for the drop of the temperature on the upper side of the radial axis (close to the wall) and also for the reduced CO_2 and CO fractions

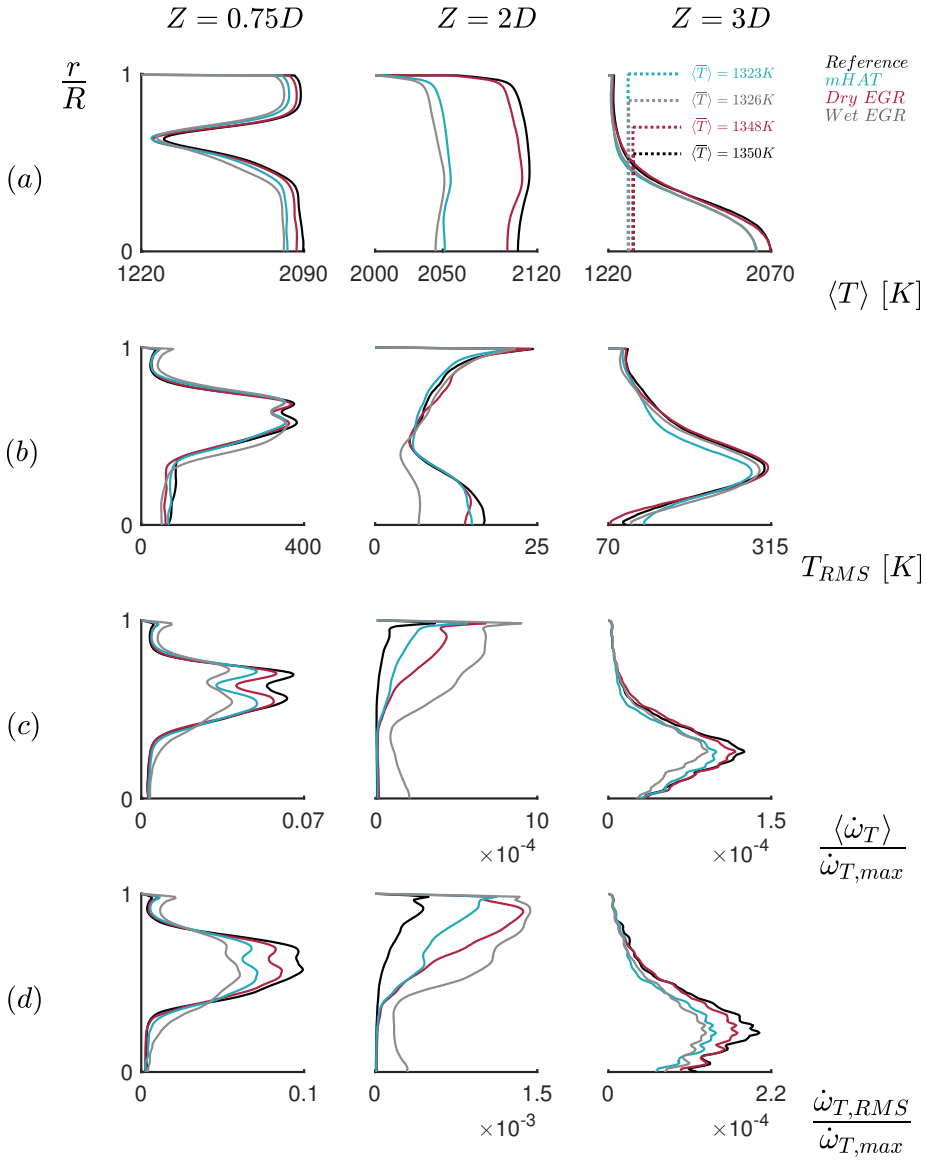

Figure 11: Comparison of azimuthal time-average temperature and reaction rate and RMS profiles for the different cases: the reference case (in black), the humidified cycle (in blue), and both dry (in red) and wet (in grey) EGR cycle in 3 positions along the chamber: in the flame front region at $Z = 0.75D$, before the DH at $Z = 2D$, at the outlet $Z = 3D$, shows that H_2O dilution involves a temperature decrease, while CO_2 dilution leads to a shift in reaction rate.

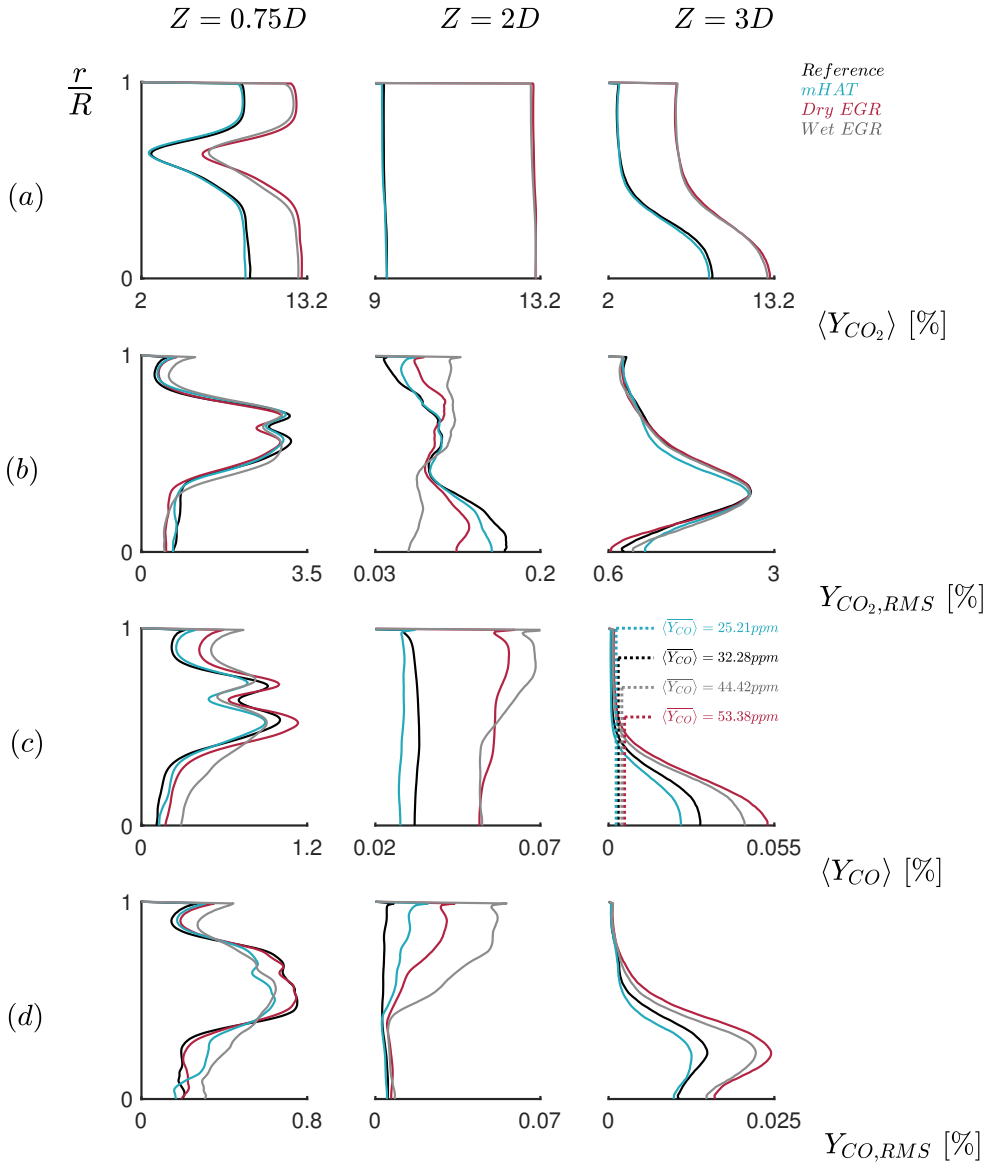

Figure 12: Comparison of azimuthal time-average CO_2 and CO and RMS profiles for the different cases: the reference case (in black), the humidified cycle (in blue), and both dry (in red) and wet (in grey) EGR cycle in 3 positions along the chamber: in the flame front region at $Z = 0.75D$, before the DH at $Z = 2D$, at the outlet $Z = 3D$, shows that CO_2 remains mostly constant, while there is a negative effect on CO due to CO_2 dilution.

(Fig. 12 (a) and (c)). Clearly, this dilution air does not penetrate to the centerline, since the temperature, CO_2 and CO fractions are still constant in this region.

Moreover, the temperature profiles (Fig. 11 (a)) are consistent with the velocity flow fields (Fig. 8 (a)). Indeed, the temperature drop at $Z = 0.75D$ corresponds to the region of the injection jet where a velocity peak stands out. In addition, this region corresponds to the flame front region since a peak of reaction rate can be observed in the related figure (Fig. 11 (c)). Furthermore, as global observation, the flow becomes more homogeneous and uniform along the chamber with a fall of the fluctuations at $Z = 2D$ (just before the DH) for the temperature, and in general for all quantities (Fig. 8, Fig. 11 and Fig. 12). This trend is similar for all simulated cases where a damping of the time-averaged profiles and a drastic decrease of the RMS values can be observed.

Finally, the average (in time and space) flow temperature at the outlet were calculated, indicating an approximate temperature of 1350 K is reached for the reference and dry EGR cases and 1325 K for both humid cases (as a result of the water dilution, see Table 5). These temperatures are slightly higher compared to the typical combustion outlet temperature for the Turbec T100 (1225 K) [9] which can be explained by the slightly altered layout (see section 3). The lower outlet temperature in the humidified cases is a result of the higher heat capacity values. A similar trend can be observed for the maximum temperature reached in the chamber: the reference case has the highest value and the humid EGR case has the lowest (see Table 5). These final outlet temperature results are validated using ASPEN Plus® [19], by

Table 5: Comparison of the combustion system performances on the maximum peak of temperatures, the time and space average of the temperature and the mass fractions emissions on wet basis of the CO_2, CO and UHC at the outlet of the combustor.

	Reference	mHAT	Dry EGR	Wet EGR
Max. temperature [K]	2500	2430	2415	2375
Outlet temperature [K]	1350	1323	1348	1326
$Y_{O_2}[\%]$	18	14.5	15	12
$Y_{H_2O}[\%]$	2.7	7.6	2.7	7.6
$Y_{CO_2}[\%]$	3.3	3.3	7.3	7.3
$Y_{CO}[ppm]$	32	25	53	44
$Y_{UHC}[ppm]$	115	75	100	90

performing equilibrium calculations. A discrepancy of maximum 0.6 % is observed between the outlet temperatures obtained for all cases with our LES and those obtained based on the ASPEN model from [19] with this equilibrium calculation. Despite this good agreement, our results show a difference between 5 % to 8 % with the results from De Santis et al. for the temperature of the reference and dry EGR cases [15]. This difference in temperature can be explained by the different wall cooling model considered by De Santis et al. [15], the different kinetic scheme, and the inlet conditions which are slightly different. Nevertheless, similar trends are observed and the results can be considered as correct and validated.

The maximal values of the reaction rate $\dot{\omega}_T$, expressing the instantaneous heat release of the reaction, are globally located in the flame front region at

$Z = 0.75D$ (Fig. 11 (c)). Therefore, we can assume that the major part of the reaction is achieved at the beginning of the combustion chamber near the flame front for all cases. In this respect, simulation results indicate that all the fuel is burnt after $Z = 0.75D$, and there is no remaining fuel at $Z = 2D$ and $3D$. In addition, very low values of reaction rate (0.1 %) can be observed at $Z = 3D$, meaning that the main reaction of the combustion is complete. Furthermore, the concentration of unburned hydrocarbon (UHC) is less than 0.01 % at the outlet of the combustion chamber (see Table 5). On the other hand, the impact of the dilution with CO_2 and/or water on the reaction rate itself can be observed close to the inlet (Fig. 11 (c)). The heat release in the diluted cases at $Z = 0.75D$ is lower than the heat release in the reference case, while an inverse trend can be observed when moving downstream. Besides, reactions still occur for the wet EGR case and to a lesser extent for the dry EGR case at $Z = 2D$ while the main reaction is almost finished at that point for the reference case, indicating thus that there is a wider reaction zone for the EGR cases. We can conclude that both CO_2 and to a lesser extent H_2O dilution have an effect on the heat release by delaying the reaction, leading to the largest impact for the combined dilution (wet EGR case). This lower reaction rate is mainly result of the lower available quantity of oxygen under diluted conditions, and to a lesser extent to the increased specific heat capacity due to water introduction (humid cases). Indeed, the equivalence ratio (Table 3) increases from 0.232 to 0.292, and the available oxygen in the inlet combustion air decreases (O_2 depletion) from 23 % to 17 %, involving therefore a decrease in the outlet O_2 levels from 18 % for the reference case to 12 % with water and CO_2 dilution (Table 5). Finally, it is worth to mention

that as highlighted when discussing the heat release (Fig. 6) in the previous section, dilution with CO_2 and/or H_2O leads to a stretched flame. This stretched flame, quantitatively validated by the reaction rate distribution (Fig. 11 (c)), involves a larger reaction zone compared to the reference case, limiting the local maximal temperature. Although no NO_x calculation have been included in these LES, based on this local reduced temperature, we can presume that NO_x emissions will be lower as a result of the dilution.

When looking at the specific CO_2 mass fractions, we can observe that the results show similar trends along the radial axis of the combustion chamber (Fig. 12 (a)), as well as no significant impact of the dilution on the time-variation (Fig. 12 (b)). As previously explained, both dry and humid EGR cases result in higher CO_2 levels in the exhaust gases. Since these cases operate with a higher CO_2 in the combustion air entering the chamber, outgoing levels are higher. Correcting for the initial 4 % CO_2 in the combustion air as a results of the flue gases recirculation in the EGR cases, the same concentration profile of CO_2 emissions are reached for all cases. Based on our quantitative results, we can conclude that water does not have any effect on CO_2 emissions, as well as EGR with CO_2 dilution either (as for the qualitative results). Obviously, given the selected operating conditions of working at constant power input combined with a combustion efficiency not impacted by the water additions (reflected in the low CO emissions, as presented before), we observe similar CO_2 emissions for both dry and wet case. As long as water addition does not lead to a significant increase in CO emissions, combustion is complete, and all fuel is converted in CO_2. However, it is expected that higher H_2O dilution will lead to a significant impact on combustion efficiency and CO emissions.

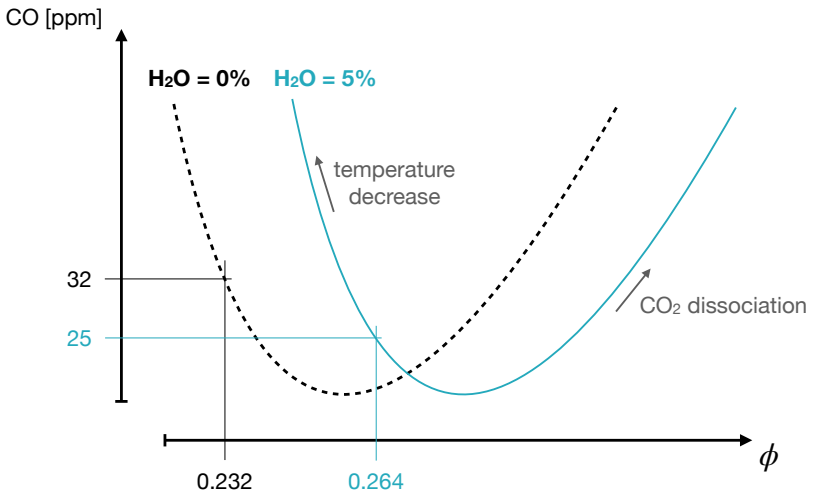

Figure 13: Generic representation of the oxygen depletion and humidification impact on the CO emissions in lean premixed swirled combustion.

Regarding the evolution of the CO mass fraction in the chamber, in general, the CO levels are relatively low in the chamber. For all cases, maximum values ($\sim$1 %) are reached in the reaction zones at $Z = 0.75D$ (areas where the reaction rate is higher), and significantly lower at the outlet of the chamber (Fig. 12 (c)). When moving down the chamber ($Z = 2D$), the CO levels decrease to very low levels which ensures complete and stable combustion for all cases, while the dilution air also helps to decrease further the CO emissions ($Z = 3D$). Furthermore, the lowest average (in time and space) value of CO at the outlet is reached in the mHAT case with 25 ppm whereas the highest values are reached for both EGR cases, and more particularly for the dry EGR case at the outlet with 53 ppm (see Fig. 12 (c) at $Z = 3D$ and Table 5 for the detailed comparison).

We observe thus that the CO concentration level slightly decreases with

humidification, which might appear counter-intuitive and in contrast with literature [49]. However, as highlighted in Fig. 13, the CO concentration levels evolve as followed: starting from lean conditions (left hand side of the curve), the CO emissions progressively decreases with increasing equivalence ratio resulting in a higher temperature reducing the risk of incomplete combustion. Then, the CO level passes by a minimum before increasing again when operating conditions become richer (right hand side of the curve). The temperature increases further involving a raise of CO concentration caused by the dissociation of the CO_2. Hermann et al. showed that water introduction leads to a shift of this operating curve, and thus a shift of the equivalence ratio [50]. In addition to this trend, Li et al. [49] and De Paepe et al. [51], showed also that the CO emissions globally increase with high humidification. Nevertheless, complete combustion and low CO levels (as low as for classical dry combustion) can be kept under humidification conditions, if the combustion operates in the appropriate equivalence ratio region and the humidification is below 30 % (as seen in Fig 13), explaining the reduction in CO levels [25]. Regarding both dry and wet EGR cases, the results show that CO concentration levels are higher compared to those of the reference case. Therefore, in our LES results, the CO level reduction of the mHAT case is mainly due to the equivalence ratio shift, resulting of the humidification as shown in Fig. 13, and to a lesser extent to the higher heat capacity (and thus lower temperature)) due to the water addition. As validated by De Santis et al. [15], less oxygen is available when CO_2 is recirculated in the cycle, involving less CO oxydation. Although the increase of CO_2 in the combustion air composition has a negative effect on the CO emissions, the results showed

that humidification can partly compensate this increase of CO level.

It is important to note that a proper experimental validation of the flame region would be necessary to fully validate the LES results. However, this is unfortunately technically impossible, and never achieved on a real facility of a complete running mGT since there is no option for optical access, nor for a detailed measurement of temperature (inside and at the outlet of the combustor), species and velocities in the combustion chamber of the mGT. The only possibility of validation lies in the comparison of our LES results on the combustor outlet conditions with other validated numerical or experimental results of the outlet conditions of the mGT cycle, in terms of CO levels. Even though there are also some technical limitations to obtain these experimental validations, depending on the studied case, we are more interested in the evolution between the different cases, allowing a partial validation.

- For the reference case, although our simulated CO emission values are already relatively low (32 ppm), the data-sheet of the Turbec T100 manufacturer announces less than 15 ppm of CO emissions, while the simulation results of De Santis et al. [15] (using RANS) show 2 ppm for the reference case and 5 ppm for the EGR case. The slight higher obtained results for the CO levels of the reference case find their origin, as explained before, in the overestimation induced by the TFLES model. However, comparison with the limited available data show that our results are within a realistic range for the reference and the EGR cases.

- For the humidified mGT case (mHAT), essentially numerical results on the impact of humidification on the mGT cycle and performances can be found in literature [32, 12, 10, 52]. Nevertheless, we have shown

(Fig. 13) that the same trends are observed with our results as those presented by Li et al. [49], even though their experimental work is more on a generic set-up, where they aim to assess the general impact of humidification on combustion.

- Regarding the dry EGR case, literature [16, 18] and authors experience [20] have shown that EGR is really difficult to emulate on a real test rig, and still too barely developed on a real mGT facility. Nevertheless, the work of Best et al. [18], which shows a configuration close to our case, present a set-up of the T100 which emulates EGR by adding CO_2 to the combustion air. Even though the operating conditions are slightly different and the aim of the work of Best et al. [18] is to assess the mechanical and cycle performances when performing EGR up to 6.3vol% of CO_2 added, the paper shows an evolution of an increase from 45% to 55% of CO emissions when EGR is performed compared to pure natural gas combustion, while our results show an increase of the CO emissions of 39%.

- Finally, for the wet EGR case, this configuration has only been studied numerically so far, and there is no available test rigs that would allow for experimental validation. Only trends of the combination of both humidification and EGR, as shown by Giorgetti et al. [21] (only for a limited operating range), can be discuss but no real validation are available.

In addition to all these considerations, even if an actual full operational mHAT-EGR test rig would be available, it would unfortunately be impossible

to simulate exactly the operating conditions as used in this paper on the test rig, considering the complex impact of the control system as well as all other cycle components (i.e. compressor, recuperator, turbine) on the combustor inlet conditions in a real system. Indeed, on an actual test rig, it is challenging to keep both combustor inlet air mass flow rate and temperature constant, when applying humidification and/or EGR. Due to the coupling of the combustion chamber with the compressor/turbine system, water addition leads to lower incoming air mass flow rate under normal operating conditions, imposed by the turbine. Moreover, given that mGTs operate at constant TOT, altering the combustion air composition by EGR and/or humification, leads to lower combustor inlet temperature, due to the changing effectiveness of the recuperator. In conclusion, even though recreating the conditions of the simulations (constant combustor inlet temperature) for an experimental validation appears as impossible, and considering the technical limitations to obtain experimental data, we can consider that the presented results of our simulations are within a realistic range of their observed values, and thus partially validated by the available data for the reference, the mHAT and the dry EGR cases.

6. Conclusion

To improve the mGT cycle by implementing advanced cycle modifications, including humidification for increased operational flexibility and EGR for carbon capture facilitation, stable and complete combustion has to be achieved under unconventional, diluted conditions. In this framework, four different operating conditions of mGT combustion chamber have been studied using an

LES approach in this paper. The considered cases include a classical typical recuperated cycle (reference case), and advanced mGT cycles modification such as: a humidified cycle using a saturation tower (mHAT), a dry cycle with EGR and a humidified cycle with EGR (mHAT+EGR).

The results presented in this paper show that complete and stable combustion was reached for all different operating conditions. Although the stability and the flame topology analysis showed that the flow dynamics is identical for all cases, the reaction still occurs further downstream of the injectors in the combustion chamber for the humid EGR conditions (water and CO_2 dilution), and to a lesser extent in both dry EGR and humid conditions. The flame topology is thus not similar for all cases, resulting in a wider reaction zone for the diluted cases. Furthermore, the temporal analysis of the heat release fluctuations confirmed that stable combustion is achieved for all cases.

Next to the qualitative analysis, a more quantitative analysis was performed focussing on temperature, heat release, and emissions. In terms of final outlet conditions, the lower outlet temperature is reached in the humidified cases (mHAT with 1323 K and Wet EGR with 1326 K), as a result of the higher specific heat capacity of the gases due to the higher water content. Those values are close to the typical values of the Turbec T100, and are validated by ASPEN simulations with a maximum discrepancy of 0.6 %.

The CO_2 levels for both EGR cases are higher compared to the dry and mHAT cases, due to the higher CO_2 content in the combustion air. Regarding the CO emissions, the mHAT case displays slightly lower emission levels (25 ppm) compared to the reference case (32 ppm) while both dry and wet EGR cases show the highest values (approximately 50 ppm). This lower level

is mainly due to the equivalence ratio shift of the humid case, and at a lesser extent to the higher heat capacity. Therefore normal level of CO emissions can be reached with humidification, if the combustion operates in the appropriate equivalence ratio range. Although the increase of CO_2 in the combustion air composition has a negative effect on the CO emissions, the results showed that humidification can partly compensate this increase. Nevertheless, the considered dilutions were relatively limited (5 % H_2O and 4 % CO_2).

Based on high fidelity LES results, the feasibility and flexibility of mGT combustor operating in diluted conditions (with water and/or CO_2) as those currently found in more advanced mGT cycles have been demonstrated. These results allow to help future combustor design towards more stability. Future work involves experimental investigations in this combustion chamber for validation, and extending the study to higher dilution rates. This next step would lead to the establishment of the performance curve of the oxygen depletion to predict the CO levels for a range of operating condition A 1D reactor approach will help to quantify the limits, while these limits will be then validated with LES simulations.

Acknowledgment

The investigations presented in this paper have been achieved thanks to the facilities of the Consortium des Equipements de Calcul Intensif (CECI) funded by the Fond de la Recherche Scientifique de Belgique (FRS-FNRS) under convention 2.5020.11. The authors thank also G. Lartigue and V. Moureau for providing the code YALES2.

Nomenclature

Acronyms

CCUS Carbon Capture Utilisation & Storage

CHP Combined Heat and Power

DH Dilution Holes

EGR Exhaust Gas Recirculation

LES Large Eddy Simulation

mGT micro Gas Turbine

mHAT micro Humid Air Turbine

RANS Reynolds-Averaged Navier-Stokes

RMS Root Mean Square

TIT Turbine Inlet Temperature

TKE Turbulent Kinetic Energy

TOT Turbine Outlet temperature

Greek symbols

δ_L^0 laminar thermal flame thickness, m

$\dot{\omega}_T$ heat release, W·$(m^3)^{-1}$

ϕ equivalence ratio

ρ density, $\mathrm{kg \cdot m^{-3}}$

Symbols

$\dot{m}$ mass flow rate, $\mathrm{kg \cdot s^{-1}}$

$d_{inj,air}$ diameter of the pilot injectors for air, m

$d_{inj,fuel}$ diameter of the pilot injectors for fuel, m

$d_{inj,main}$ diameter of the main injectors, m

y^+ dimensionless wall distance

D diameter of the combustion chamber, m

E efficiency function

F thickening factor

G_θ tangential momentum, $\mathrm{kg \cdot m \cdot s^{-1}}$

G_z axial momentum flux, $\mathrm{kg \cdot m \cdot s^{-1}}$

Re Reynolds number

S Swirl number

S_L^0 laminar flame speed, $\mathrm{m \cdot s^{-1}}$

T temperature, K

u velocity, $\mathrm{m \cdot s^{-1}}$

u_θ tangential velocity, $\mathrm{m \cdot s^{-1}}$

u_z axial velocity, $m \cdot s^{-1}$

Y_k mass fraction of the species k

References

[1] International Energy Agency, World energy outlook 2018, Tech. rep., International Energy Agency (IEA).

[2] United Nations (UNFCCC), Paris agreement, Tech. rep., United Nations (2015).

[3] T. Bayar, Microturbines take on the market, Power Engineering International, Cogeneration and on-site power production (2015).

[4] S. Gamou, K. Ito, R. Yokoyama, Optimal operational planning of cogeneration systems with microturbine and dessicant air conditioning units, Journal of Engineering for Gas Turbines and Power 127(3) (2005) 606–614.

[5] P. Pilavachi, Mini- and micro-gas turbines for combined heat and power, Applied Thermal Engineering 22 (18) (2002) 2003 – 2014.

[6] U. S. Department of Energy, Advanced microturbine systems - program plan for fiscal years 2000 through 2006, in: Office of Energy Efficiency and Renewable Energy and Office of Power Technologies, 2000.

[7] Frost & Sullivan, Combined heat and power: Integrating biomass technologies in buildings for efficient energy consumption (2011).

[8] M. Montero Carrero, W. De Paepe, J. Magnusson, A. Parente, S. Bram, F. Contino, Experimental characterisation of a micro humid air turbine: assessment of the thermodynamic performance, Applied Thermal Engineering 118 (2017) 796 – 806.

[9] Turbec, T100 microturbine CHP system: Technical description version 4.0 (2010-2011).

[10] M. Montero Carrero, W. De Paepe, S. Bram, F. Musin, A. Parente, F. Contino, Humidified micro gas turbines for domestic users: An economic and primary energy savings analysis, Energy 117 (2016) 429 – 438.

[11] P. Stathopoulos, C. Paschereit, Operational strategies of wet cycle micro gas turbine and their economic evaluation, ASME J. Eng. Gas Turbines Power 138(2) (2015) 122301.

[12] W. De Paepe, M. Montero Carrero, S. Bram, A. Parente, F. Contino, Toward higher micro gas turbine efficiency and flexibility humidified micro gas turbines: A review, Journal of Engineering for Gas Turbines and Power 140 (8) (2018) 146–154.

[13] W. De Paepe, M. Montero Carrero, S. Bram, F. Contino, T100 micro gas turbine converted to full humid air operation: A thermodynamic performance analysis, in: ASME Turbo Expo 2015: GT2015-43267, 2015, p. V003T06A015.

[14] M. Montero Carrero, W. De Paepe, J. Magnussen, A. Parente, S. Bram, F. Contino, Experimental characterisation of a humidified t100 micro

gas turbine, in: ASME Turbo Expo 2016: GT2016-57649, 2016, p. V003T06A016.

[15] A. De Santis, D. B. Ingham, L. Ma, M. Pourkashanian, CFD analysis of exhaust gas recirculation in a micro gas turbine combustor for CO2 capture, Fuel 173 (2016) 146–154.

[16] M. Cameretti, R. Piazzesi, F. Reale, R. Tuccillo, Combustion simulation of an exhaust gas recirculation operated micro-gas turbine, Journal of Engineering for Gas Turbines and Power 131 (5) (2009) 051701.

[17] U. Ali, T. Best, K. N. Finney, C. F. Palma, K. J. Hughes, D. B. Ingham, M. Pourkashanian, Process simulation and thermodynamic analysis of a micro turbine with post-combustion CO2 capture and exhaust gas recirculation, Energy Procedia 63 (2014) 986 – 996.

[18] T. Best, K. N. Finney, D. B. Ingham, M. Pourkashanian, Impact of CO2-enriched combustion air on micro-gas turbine performance for carbon capture, Energy 115 (2016) 1138 – 1147.

[19] W. De Paepe, M. Montero Carrero, S. Giorgetti, A. Parente, S. Bram, F. Contino, Exhaust gas recirculation on humidified flexible micro gas turbines for carbon capture applications, in: ASME Turbo Expo 2016: GT2016-57265, 2016, p. V003T06A011.

[20] S. Giorgetti, L. Bricteux, A. Parente, J. Blondeau, F. Contino, W. De Paepe, Carbon capture on micro gas turbine cycles: Assessment of the performance on dry and wet operations, Applied Energy 207 (2017) 243 – 253.

[21] S. Giorgetti, A. Parente, F. Contino, L. Bricteux, W. De Paepe, Humidified micro gas turbine for carbon capture applications: Preliminary experimental results with CO2 injection, in: ASME Turbo Expo 2018: GT2018-77265, 2018, p. V003T06A024.

[22] W. De Paepe, M. Renzi, M. Montero Carrero, C. Caligiuri, F. Contino, Micro gas turbine cycle humidification for increased flexibility: Numerical and experimental validation of different steam injection models, in: ASME Turbo Expo 2018: GT2018-76696, 2018, p. V003T06A018.

[23] S. Goke, M. Furi, G. Bourque, B. Bobusch, K. Gockeler, O. Kruger, S. Schimek, S. Terhaar, C. O. Paschereit, Influence of steam dilution on the combustion of natural gas and hydrogen in premixed and rich-quench-lean combustors, Fuel Processing Technology 107 (2013) 14 – 22.

[24] S. Lellek, T. Sattelmayer, Influence of water injection on heat release distribution, lean blowout and emissions of a premixed swirl flame in a tubular combustor, in: ASME Turbo Expo 2015: GT2015-42602, 2015, p. V04AT04A046.

[25] A. N. Mazas, D. A. Lacoste, T. Schuller, Experimental and numerical investigation on the laminar flame speed of CH4/O2 mixtures diluted with CO2 and H2O, in: ASME Turbo Expo 2010: GT2010-22512, 2010.

[26] S. Giorgetti, A. Parente, L. Bricteux, F. Contino, W. D. Paepe, Optimal design and operating strategy of a carbon-clean micro gas turbine for com-

bined heat and power applications, International Journal of Greenhouse Gas Control 88 (2019) 469 – 481.

[27] A. Pappa, B. Bricteux, P. Bénard, W. De Paepe, Can water dilution avoid flashback on a hydrogen enriched micro gas turbine combustion? a large eddy simulations study, Journal of Engineering for Gas Turbine and Power 143 (2020) 041008.

[28] A. Pappa, M. Cordier, P. Bénard, L. Bricteux, W. De Paepe, How far can we go? stability assessment of micro gas turbine combustion under diluted condition using LES, in: 9th European Combustion Meeting (ECM), Lisboa, Portugal, 2019.

[29] W. De Paepe, F. Delattin, S. Bram, J. De Ruyck, Steam injection experiments in a microturbine - a thermodynamic performance analysis, Applied Energy 97 (2012) 569 – 576.

[30] T. Zornek, T. Monz, M. Aigner, Performance analysis of the micro gas turbine turbec T100 with a new flox-combustion system for low calorific fuels, Applied Energy 159 (2015) 276–284.

[31] A. Schwarzle, T. O. Monz, M. Aigner, Detailed examination of two-staged micro gas turbine combustor, in: ASME Turbo Expo 2016: GT2016-57730, 2016, p. V04BT04A039.

[32] W. De Paepe, M. Montero Carrero, S. Bram, F. Contino, A. Parente, Waste heat recovery optimization in micro gas turbine applications using advanced humidified gas turbine cycle concepts, Applied Energy 207 (2017) 218 – 229.

[33] V. Moureau, P. Domingo, L. Vervisch, Design of a massively parallel CFD code for complex geometries, Comptes Rendus Mecanique 339 (2-3) (2011) 141–148.

[34] M. Kraushaar, Application of the compressible and low-mach number approaches to large-eddy simulation of turbulent flows inaero-engines, Ph.D. thesis, CERFACS (2011).

[35] P. Bénard, V. Moureau, G. Latrigue, Y. D'Angelo, Large-eddy simulation of a hydrogen enriched methane/air meso-scale combustor, International Journal of Hydrogen Energy 42 (4) (2011) 2397–2410.

[36] L. Boulet, P. Bénard, G. Lartigue, V. Moureau, S. Didorally, N. Chauvet, F. Duchaine, Modeling of conjugate heat transfer in a kerosene/air spray flame used for aeronautical fire resistance tests, Flow, Turbulence and Combustion 101 (2) (2018) 579–602.

[37] P. Bénard, G. Lartigue, V. Moureau, R. Mercier, Large-eddy simulation of the lean-premixed preccinsta burner with wall heat loss, Proceedings of the Combustion Institute 37 (4) (2019) 5233 – 5243.

[38] M. Germano, U. Piomelli, P. Moin, W. Cabot, A dynamic subgridscale eddy viscosity model, Physics of Fluids 3 (7) (1991) 1760–1765.

[39] S. B. Pope, Turbulent Flows, 3rd Edition, Cambridge University Press, 2000.

[40] A. Kazakov, M. Frenklach, DRM19 mechanism.

[41] G. Smith, D. Golden, M. Frenklach, N. Moriarty, B. Eitneer, M. Goldenberg, C. Bowman, R. Hanson, S. Song, W. Gardiner Jr, et al., GRI3.0 mechanism, in: Gas Research Institute, 1999.

[42] O. Colin, F. Ducros, D. Veynante, T. Poinsot, A thickened flame model for large eddy simulations of turbulent premixed combustion, Physics of Fluids 12 (7) (2000) 1843–1863.

[43] F. Charlette, C. Meneveau, D. Veynante, A power-law flame wrinkling model for les of premixed turbulent combustion part ii: dynamic formulation, Combustion and Flame 131 (1) (2002) 181 – 197.

[44] T. Poinsot, D. Veynante, Theoretical and Numerical Combustion, 3rd Edition, Cambridge University Press, 2001.

[45] J. P. Légier, T. Poinsot, B. Varoquié, F. Lacas, D. Veynante, Large eddy simulation of a non-premixed turbulent burner using a dynamically thickened flame model, in: A. Pollard, S. Candel (Eds.), IUTAM Symposium on Turbulent Mixing and Combustion, Springer Netherlands, Dordrecht, 2002, pp. 315–326.

[46] P. Schmitt, T. Poinsot, B. Schuermans, K. P. Geigle, Large-eddy simulation and experimental study of heat transfer, nitric oxide emissions and combustion instability in a swirled turbulent high-pressure burner, Journal of Fluid Mechanics 570 (2007) 17–46.

[47] D. Durox, J. P. Moeck, J.-F. Bourgouin, P. Morenton, M. Viallon, T. Schuller, S. Candel, Flame dynamics of a variable swirl number

system and instability control, Combustion and Flame 160 (9) (2013) 1729 – 1742.

[48] P. Balakrishnan, K. Srinivasan, Influence of swirl number on jet noise reduction using flat vane swirlers, Aerospace Science and Technology 73 (2018) 256 – 268.

[49] M. Li, Y. Tong, M. Thern, J. Klingmann, Influence of the steam addition on premixed methane air combustion at atmospheric pressure, Energies 10 (2017).

[50] F. Hermann, J. Klingmann, R. Gabrielsson, Computational and experimental investigation of emissions in a highly humidified premixed flame, in: ASME Turbo Expo 2003: GT2003-38337, 2003.

[51] W. De Paepe, P. Sayad, S. Bram, J. Klingmann, F. Contino, Experimental investigation of the effect of steam dilution on the combustion of methane for humidified micro gas turbine applications, Combustion Science and Technology 188 (8) (2016) 1199 – 1219.

[52] M. Montero Carrero, W. De Paepe, S. Bram, F. Contino, Thermodynamic analysis of water injection in a micro gas turbine: Sankey and grassmann diagrams, Energy Procedia 105 (2017) 1414 – 1419.